Assessment of Transition Model and CFD Methodology for Wind Turbine Flows

Aniket C. Aranake[*]   Vinod K. Lakshminarayan[†]   Karthik Duraisamy [‡]

A detailed evaluation of the predictive capability of a Reynolds Averaged Navier Stokes (RANS) solver with a transition model is performed for wind turbine applications. The performance of the computational methodology is investigated in situations involving attached flow as well as incipient and massive flow separation and compared with experiment. Two-dimensional simulations on wind turbine airfoil sections are seen to qualitatively and quantitatively predict the onset of transition to turbulence and provide significantly improved lift and drag predictions when compared to simulations that assume fully turbulent flow. In three-dimensional wind turbine simulations, detailed validation studies of the integrated loads and sectional pressure coefficient also show definite improvements at wind speeds at which separation is incipient or confined to a small portion of the blade surface. At low wind speeds, for which the flow is mostly attached to the blade surface, and at high wind speeds, for which it is massively separated, the transition model produces similar results to a fully turbulent calculation. Overall, the performance of the transition model highlights the necessity of such models while also pointing out the need for further development.

Nomenclature

α	Angle of attack
γ	Intermittancy
$\nu_{T\infty}$	Freestream eddy viscosity
ω	Specific dissipation
$\overline{Re_{\theta t}}$	Transition momentum thickness Reynolds number
ϕ	Blade geometric twist
ρ	Density of air
c	Chord length
c_d	Sectional drag coefficient
c_f	Skin friction coefficient
c_l	Sectional lift coefficient
C_p	Pressure coefficient
C_Q	Torque coefficient
C_T	Thrust coefficient
k	Turbulent kinetic energy
M_{FS}	Freestream Mach number
M_{tip}	Rotor tip Mach number
P	Static pressure
P_∞	Freestream static pressure
Q	Torque
R	Rotor radius
r	Rotor spanwise coordinate
Re_θ	Momentum thickness Reynolds number

[*]PhD Candidate, Department of Aeronautics and Astronautics, Stanford University, Stanford, CA.
[†]Postdoctoral Fellow, Department of Aeronautics and Astronautics, Stanford University, Stanford, CA.
[‡]Assistant Professor (Consulting), Department of Aeronautics and Astronautics, Stanford University, Stanford, CA.

Re_x	Local position Reynolds number
T	Thrust
Tu_∞	Freestream turbulence intensity
V_∞	Freestream velocity
V_{tip}	Rotor tip velocity
x_{trans}	Chordwise transition location

I. Introduction

In recent decades, wind energy's share of the global energy portfolio has been increasing, a trend which is expected to continue as fossil fuels are replaced by renewable alternatives. In the U.S., the Department of Energy has published a report outlining its plan to satisfy 20% of the national energy budget with wind power.[1] In a best case scenario, the report estimates that annual wind energy production can increase by 35% due to improvements related to aerodynamics. As technology matures, achieving these gains in performance will depend on an increasingly sophisticated understanding of physics, and thus classical engineering models reach their limit of usefulness. Higher fidelity methods, such as the one discussed in the present work, provide designers with the ability to assess the performance of their designs with high confidence. This information reduces uncertainty for businesses and promotes the development of wind energy solutions. Additionally, advanced concept designs such as diffuser augmented wind turbines (DAWTs), active flow control, and plasma actuation rely on nonlinear and interactional aerodynamic effects, so the adoption of these technologies is increasingly reliant on the availability of fast and reliable modeling tools.

The simplest models for wind turbine aerodynamic analysis use momentum theory and blade element theory which make use of the integral mass, momentum, and energy equations in a control volume around the turbine along with simple aerodynamic models or tabulated airfoil data. While such models provide some practical insight and sizing estimates, they are of limited use in the design of modern wind turbines. An introduction to low-order wind turbine aerodynamics including details of these methods can be found in Hansen.[2] More sophisticated techniques to include the effects of the evolving wake system of turbines and to include unsteady gusts or turbine yaw can be derived using vortex panel/filament based methods.[3]

In all of these methods, first order effects such as viscosity and turbulence can only be treated in a purely empirical manner. Physically accounting for these effects requires higher fidelity CFD modeling. An assessment of predictive capabilities by Simms et al.[4] revealed that different models produce widely varying results. Experimental data from this study, the NREL Phase VI Rotor Unsteady Aerodynamics Experiment, was published[5] and has since been used to assess wind turbine aerodynamic models in several publications (see, for example, Sørensen et al.,[6] Duque et al.,[7] Potsdam et al.[8])

A principal difficulty in the accurate simulation of wind turbine aerodynamics is an accurate representation of separated flow. In this regard, predicting the transition from laminar to turbulent flow may be extremely important, especially when laminar separation bubbles (LSB) are present near the leading edge of the airfoil. In such cases, if transition occurs over the bubble, the LSB may burst, causing leading edge stall. This process may be highly sensitive to even low energy perturbations and phenomena such as the double stall phenomenon can occur.[9] A classic approach to predicting transition is the method of Michel,[10] which triggers transition based on an empirical correlation between momentum thickness Reynolds number Re_θ and Reynolds number based on local length Re_x at the point of transition. This model is sufficiently accurate for many airfoil-type problems,[11] but does not account for surface roughness. For wind turbine airfoils, a commonly used technique is that of Eppler,[12] which has been employed in the design of several NREL S-series wind turbine airfoils.[13, 14] This method, which is also empirical, incorporates a roughness factor into a comparison between integral boundary layer quantities to decide when to trigger transition. For practical problems, these methods typically involve a numerical integration of the boundary layer followed by a search for critical momentum Reynolds number, both of which can be expensive and difficult to apply in three dimensions.

An alternate approach to identifying transition is through the use of stability analysis. The Orr-Sommerfeld equations,[15] based on the linearized Navier-Stokes equations, describe when the linearized modes in parallel shear flows will amplify, causing the flow to become turbulent. This simplified view of the transition phenomenon neglects nonlinear effects, which can create large destabilizing transients. A more commonly used method is the e^n method of Smith et al.[16] and Van-Ingen.[17] These methods correlate the amplitude ratio of the largest mode to the location of transition. A shortcoming of this type of method is

American Institute of Aeronautics and Astronautics

that it requires the computation of streamlines, adding significantly to the cost and complexity of a CFD simulation. An extensive review of transition models for CFD has been published by Pasquale et al.[18]

Direct methods for the prediction of transition and separated flow such as DNS or LES are frequently prohibitively expensive for industrial applications. For this reason, a transition model augmenting the RANS equations is desirable. To further avoid the difficulties of the methods mentioned above, it is desirable to select a method that makes use of local quantities. With this property, a model can be readily implemented into an existing RANS solver. A recently published model that satisfies this criteria is the $\gamma - \overline{Re_{\theta t}}$ model by Langtry et al.[19] This model requires the solution of two transport equations in addition to the RANS equations and the SST $k - \omega$ turbulence model.[21] An investigation by the same authors[20] found that this model improves significantly the prediction of torque in wind turbine flows involving separation. However, the quality of the results is somewhat obscured by the discrepancy of the predictions with measured results in the attached flow regime. Since its development, the $\gamma - \overline{Re_{\theta t}}$ model has been adapted by Medida et al.[22] for use with the Spalart-Allmaras turbulence model.[23] Compared to popular two equation turbulence models, the Spalart-Allmaras model is more widely used in applications involving external flows, and it is also typically less expensive and more numerically well-behaved.

The objective of the current work is to carefully evaluate the applicability of RANS-based flow solver and $\gamma - \overline{Re_{\theta t}} - SA$ model for wind turbine simulations. Specific emphasis is given to transition to turbulence caused by the Laminar separation bubble. Simulations with and without the use of this transition model are performed in two dimensional airfoil flows as well as in wind turbine rotors. For simulations run without the transition model, the flow is assumed to be fully turbulent and the Spalart-Allmaras method is employed in its original form. The results are carefully validated against experimental data, and the predicted flow physics are analyzed in detail.

II.   Flow Solver

In this work, computations are performed using the overset structured mesh solver OVERTURNS.[24] This code solves the compressible RANS equations using a preconditioned dual-time scheme in the diagonalized approximate factorization framework, described by Buelow et al.[25] and Pandya et al.[26] The diagonal form of the implicit approximate factorization method was originally developed by Pulliam and Chaussee.[27] The low Mach preconditioning is based on the one developed by Turkel.[28] The preconditioning is used not only to improve convergence but also to improve the accuracy of the spatial discretization. The inviscid terms are computed using a third order MUSCL scheme utilizing Koren's limiter with Roe's flux difference splitting and the viscous terms are computed using second order central differencing. For RANS closure, the Spalart-Allmaras[23] turbulence model is employed. To the effects of flow transition, the $\gamma - \overline{RE_{\theta t}} - SA$[22] model is used. For completeness, details of the model is included in the appendix.

III.   2D Validation Results

For an initial assessment of the effectiveness of the $\gamma - \overline{Re_{\theta t}} - SA$ transition model, two-dimensional simulations are performed on two different NREL S-series airfoils, the S827 and the S809. These airfoils are widely used in wind turbines, and their physics is strongly characterized by the effects of transition.

Experimental results[13,14] are available for both airfoils at different angles of attack at a freestream Mach number of 0.1. The Reynolds number for the S827 airfoil is 3×10^6 and that for the S809 airfoil is 2×10^6. The freestream turbulence intensity is less than 0.05%. C-O type meshes are used for the simulations. The baseline grid has 527×101 points in the wrap-around and normal directions, respectively. Figure 1 shows the grid used for S827 calculation.

A.   S827 Airfoil

The S827 airfoil, used in stall-regulated wind turbines, is designed to deliberately induce flow separation beyond a prescribed angle of attack. The separated region is confined to a "separation ramp"[14] near the trailing edge of the upper surface so that the airfoil may continue to operate with reduced lift. Accordingly, a salient feature of the S827 lift curve is its two distinct slopes, one corresponding to angles below stall and a second slope for the post-stall region beginning at and angle of attack around $\alpha = 5°$. It is particularly difficult to capture this double slope behavior using RANS-based simulations, and therefore this case serves

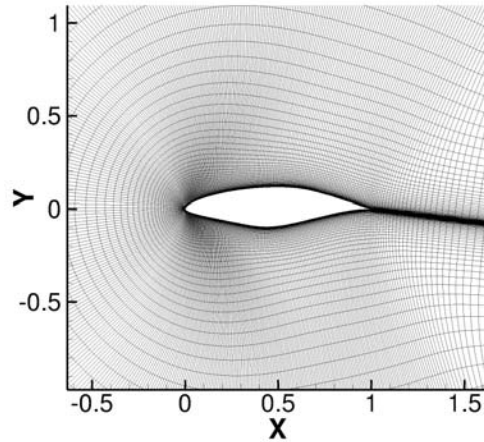American Institute of Aeronautics and Astronautics

Figure 1. Baseline grid for S827 calculation

as a good test for the transition model.

Figure 2 shows the mean lift coefficient as a function of angle of attack along with error bars representing the range of unsteady variation in the time-accurate simulations. In Fig. 2(a), the results from the simulations with and without the transition model are compared to the experimental data. The effectiveness of the transition model is evident from the plot. While the fully turbulent simulation fails to capture the double slope and predicts a much higher maximum lift coefficient as compared to the experimental value, the simulation using the transition model captures both the lift slopes as well. In addition, the transition model captures the maximum lift coefficient accurately. The only discrepancy is that the predicted angle at which the lift slope changes is 7° instead of 5°. Figure 2(b) shows the results obtained from a sensitivity study on grid refinement. The results are computed on a fine 727×101 grid and a coarse 327×85 grid. Here, the baseline grid is referred to as the medium grid. The computed lift coefficients change only slightly between the grids, giving further confidence in the results. A more detailed validation of the transition model is obtained by comparing the surface pressure coefficient distribution. Shown in Fig. 3 are the results at two angles of attack, 4° and 12°. As with the integrated lift coefficient, the use of the transition model significantly improves the quality of the solution at both angles of attack.
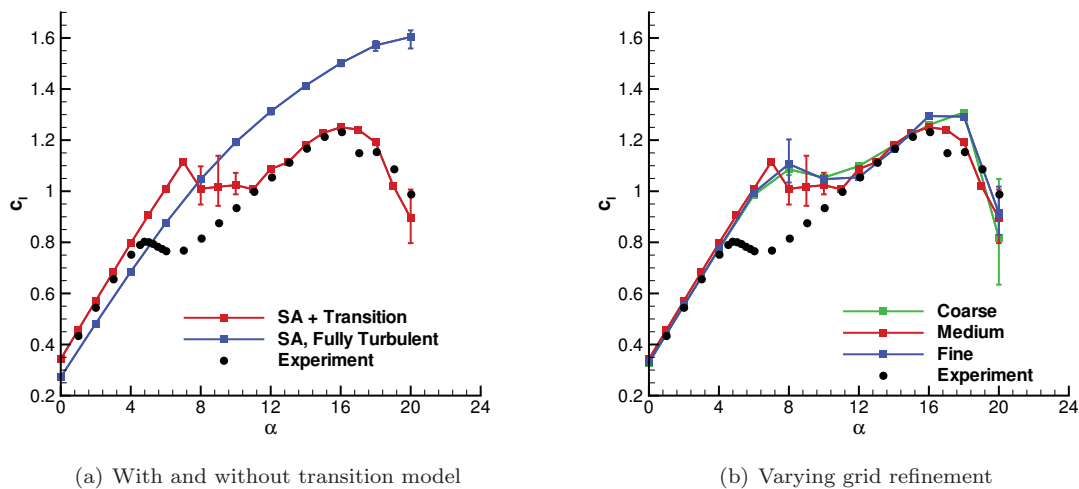

(a) With and without transition model

(b) Varying grid refinement

Figure 2. Lift coefficient vs angle of attack for S827 airfoil.

American Institute of Aeronautics and Astronautics

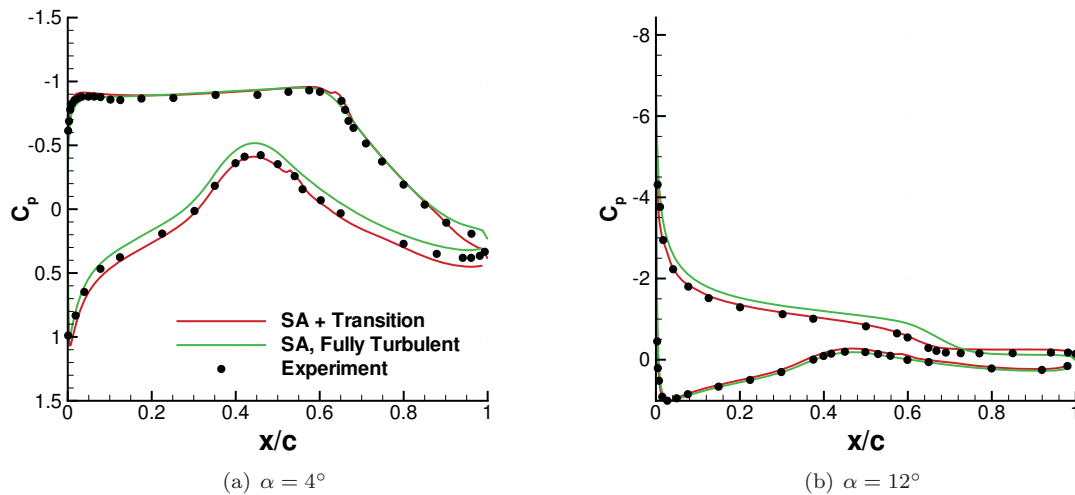(a) $\alpha = 4°$ (b) $\alpha = 12°$

Figure 3. Pressure coefficient distributions for S827 airfoil.

To further illustrate the differences between solutions obtained from fully turbulent simulations and those using the transition model, the eddy viscosity contours at 4° and 12° angles of attack are shown in Figs. 4 and 5 respectively. At 4° angle of attack, where the flow is laminar in the front half of the airfoil, the simulation using the transition model has very low levels of eddy viscosity until the transition ramp near mid-chord. The eddy viscosity then increases in the turbulent rear half of the airfoil. On the other hand, in the fully turbulent simulation the eddy viscosity begins growing in magnitude immediately from the leading edge of the airfoil, resulting in higher overall levels. At 12° angle of attack, transition is expected to occur at the leading edge of the airfoil and to separate on the aft side of the airfoil. At this angle, the eddy viscosity levels start growing at the leading edge in both the simulations, however the use of the transition model
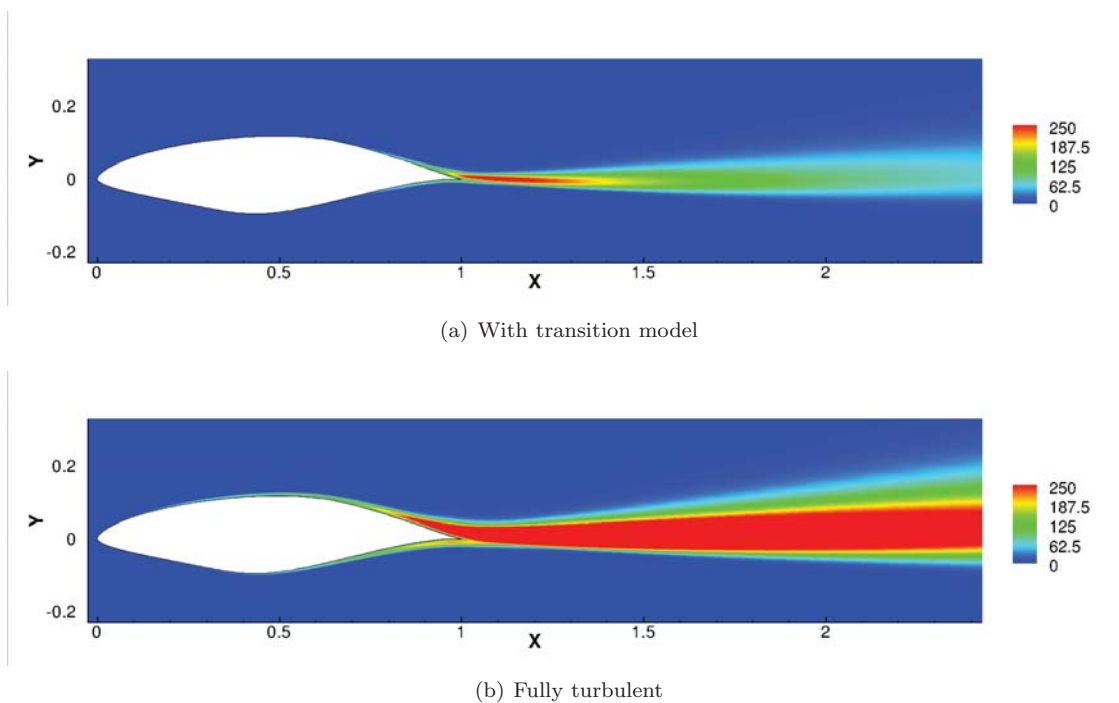

(a) With transition model

(b) Fully turbulent

Figure 4. Contours of eddy viscosity at $\alpha = 4°$ for S827 airfoil.

American Institute of Aeronautics and Astronautics

(a) With transition model

(b) Fully turbulent
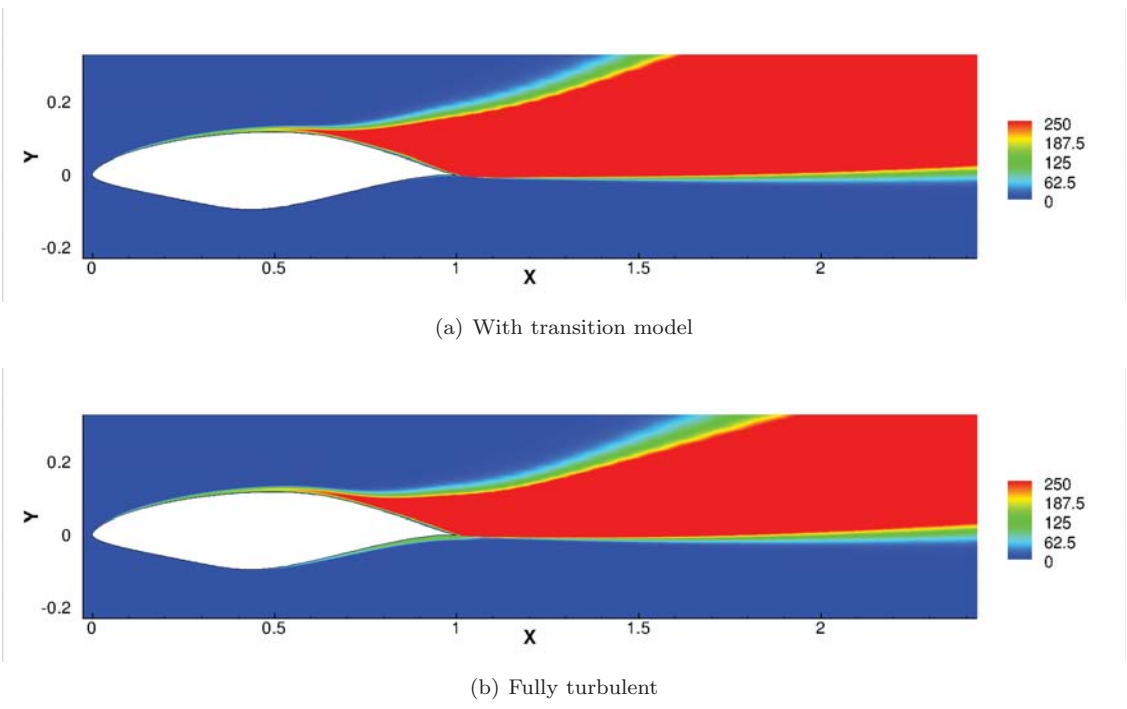
Figure 5. Contours of eddy viscosity at $\alpha = 12°$ for S827 airfoil.

(a) $\alpha = 4°$

(b) $\alpha = 12°$
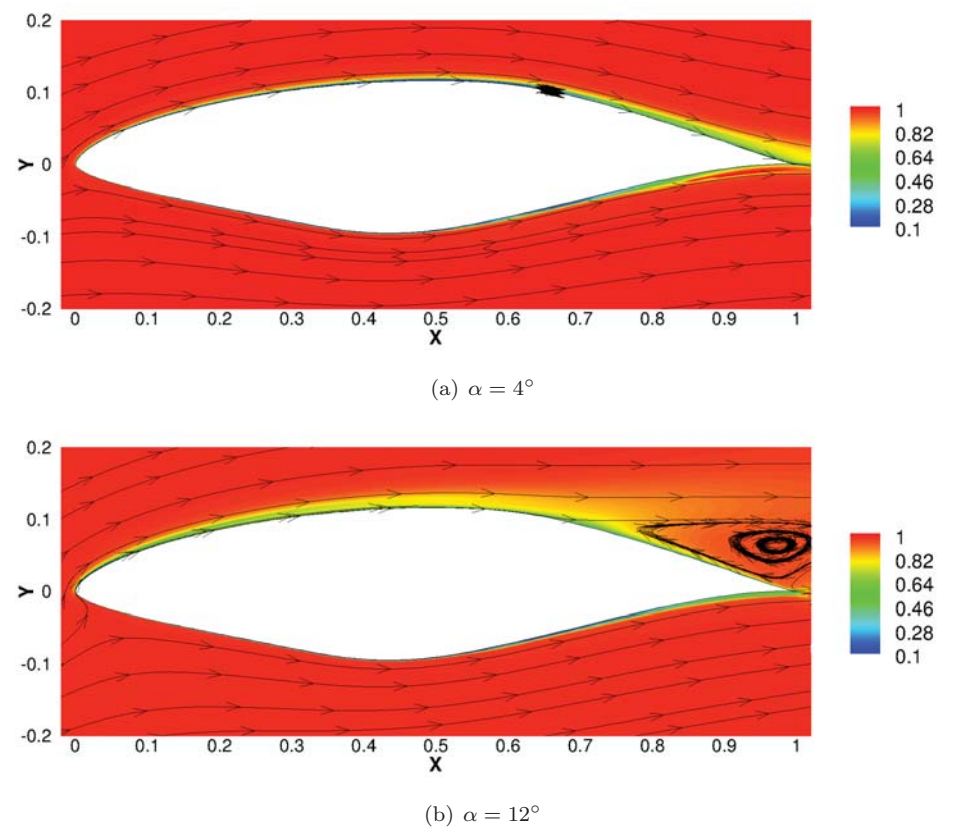
Figure 6. Contours of intermittency with streamlines for S827 airfoil.

American Institute of Aeronautics and Astronautics

(a) Variation with freestream turbulence intensity

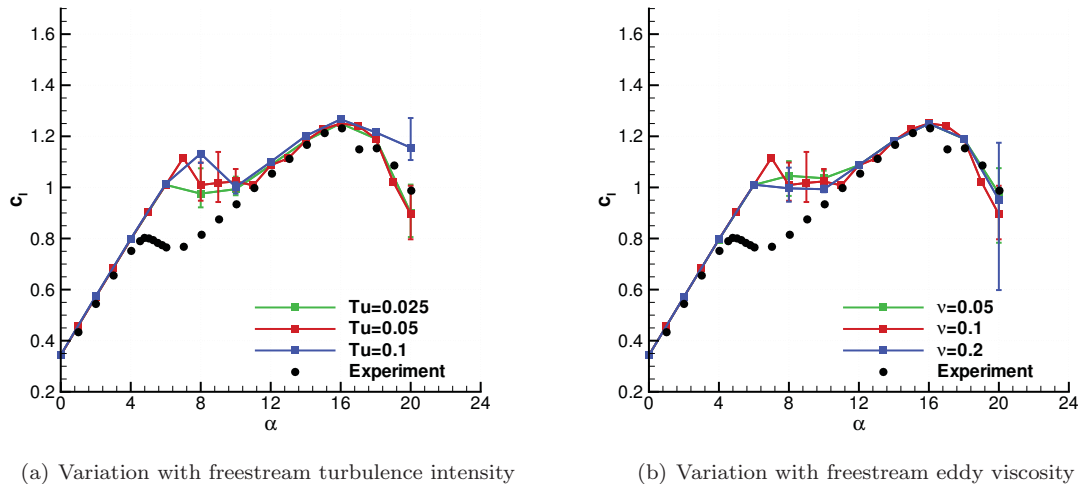(b) Variation with freestream eddy viscosity

Figure 7. Lift coefficient vs angle of attack for S827 airfoil.

shows a lower growth rate. As a result, the transition model predicts lower viscous damping which leads to increased separation in the aft of airfoil. When the flow separates, the simulation using the transition model shows higher levels of eddy viscosity.

The behavior of the transition model is further exemplified by contours of intermittency, which are shown along with velocity streamlines in Fig. 6. Intermittency is a factor that directly affects the production of eddy viscosity; values less than one indicate decreased production, while a value of one restores production to that of the fully turbulent Spalart-Allmaras model. At both angles of attack, the intermittency values are below one near the airfoil surface, but when the flow separates at 12° angle of attack, the intermittency increases rapidly. The velocity streamlines indicate the presence of a small separation bubble at the 67% chord location at 4° angle of attack, as well as the large separated region on the upper surface at 12° angle of attack.

It is also critical to understand the sensitivities of the flow solution to freestream turbulence intensity (Tu_∞) and freestream eddy viscosity ($\nu_{T\infty}$), since these quantities can be expected to vary significantly in an actual wind turbine environment. Figures 7(a) and 7(b) show the effect of perturbations to these parameters on lift coefficient. The lift is found to be reasonably insensitive to these parameters for the chosen range of values.

B.   S809 Airfoil

The S809 airfoil is used in the NREL Phase VI wind turbine, against which the 3D solver is validated. For this reason, a 2D validation study is performed on this airfoil prior to 3D simulations. Similar to the S827 airfoil, the downstream half of the top surface of this airfoil is designed to have a "transition ramp,"[13] an extended region of gentle pressure recovery which encourages the smooth transition of flow from laminar to turbulent.

Results for lift coefficient and drag coefficient of the S809 airfoil are shown in Figure 8. Again the $\gamma - \overline{Re_{\theta t}} - SA$ model significantly improves the prediction of both quantities, particularly in the post-stall region. The use of the transition model is also seen to predict the pressure coefficient accurately (Fig. 9). Notably, the transition model correctly captures the dip in pressure distribution which indicates the location of transition.

The transition locations for each angle of attack are plotted in Figure 10. Transition is triggered by laminar separation bubbles, which span several grid points in the CFD solutions. Error bars are used to represent the location and width of these bubbles. The transition locations are captured well except in the range between $\alpha = 6°$ and $\alpha = 8°$ on the upper surface of the airfoil. The calculations predict that the separation bubble on the upper surface jumps to the leading edge of the airfoil at $\alpha = 9°$. The flow near the surface was found to be volatile in the middle range of angles and highly sensitive to small disturbances.
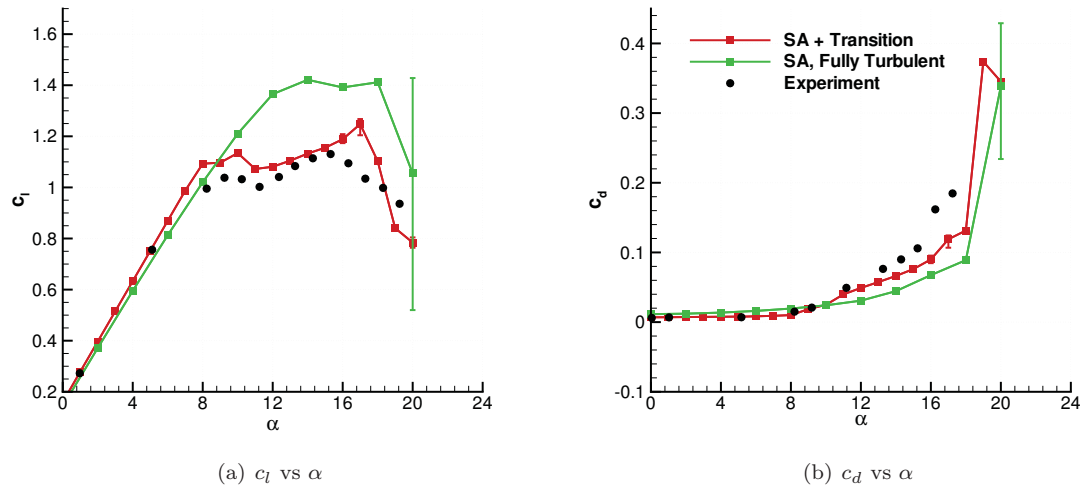
American Institute of Aeronautics and Astronautics

(a) c_l vs α (b) c_d vs α

Figure 8.   Lift and drag coefficients vs angle of attack for S809 airfoil.

(a) $\alpha = 4°$ (b) $\alpha = 12°$
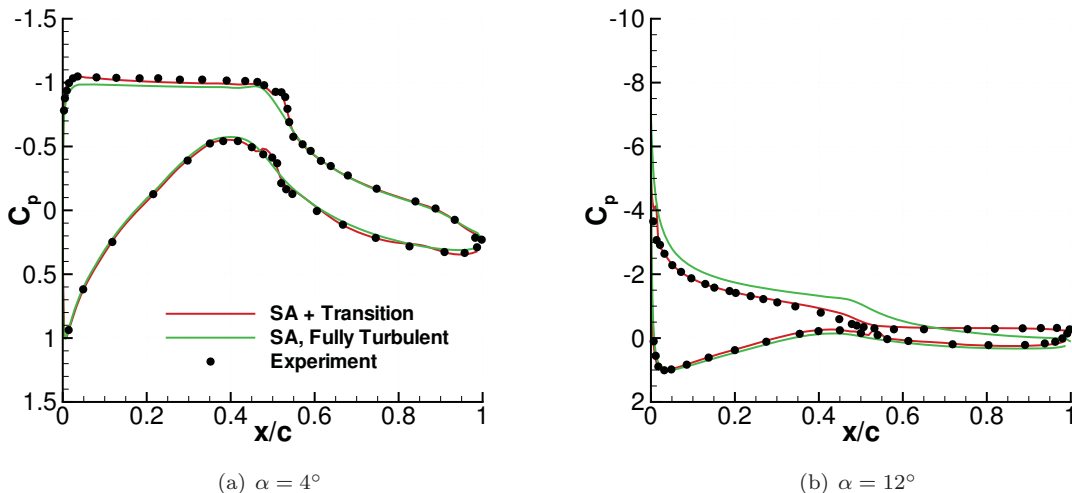
Figure 9.   Pressure coefficient distribution for S809 airfoil.

IV.   3D Validation Results

The performance of the $\gamma - \overline{Re_{\theta t}} - SA$ transition model and three dimensional solver are assessed against experimental data available from the NREL Phase VI Unsteady Aerodynamics Experiment (UAE).[5] The configuration is a two-bladed wind turbine consisting of S809 airfoil sections. The blade radius is $R = 5.029$ m and the chord length is tapered from $c = 0.737$ m to $c = 0.305$ m. The blade twist varies from $\phi = 20°$ to $\phi = -2.5°$ from root to tip. A detailed geometric description, including the distributions of twist and taper at spanwise locations, is provided in the UAE report. The blade is rotated at an RPM of 72 and the tip Reynolds number is 2.42×10^6. Data is available for wind speeds ranging from 7 m/s to 25 m/s

The computations are performed on an overset mesh system consisting of a C-O type blade mesh and a background mesh. To reduce computational cost, the simulations are performed in a half-cylinder background mesh with periodic boundary conditions to represent a cylindrical domain. Information is exchanged between the meshes using Chimera interpolations. An implicit hole-cutting technique developed by Lee[29] and improved by current authors[24] is used to determine the connectivity information between various overset meshes. The blade mesh has $257 \times 51 \times 51$ points in the wrap-around, spanwise and normal directions,
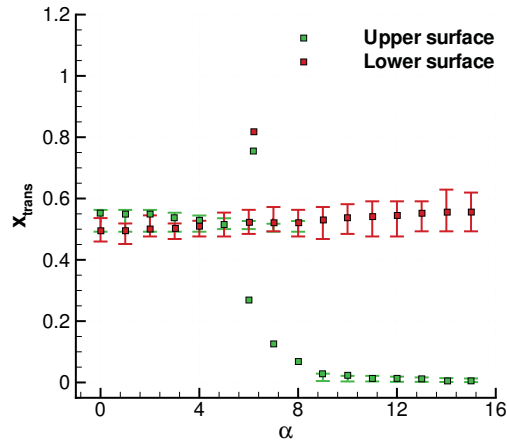
Figure 10. Transition locations for S809 airfoil. The square symbols in this plot are experimental data points. Error bars show the size of the separation bubble in CFD solution.

respectively. The background mesh has $201 \times 133 \times 164$ in the azimuthal, radial, and axial directions, respectively, with azimuthal refinement in a $15°$ patch encompassing the blade. The most refined part of the background mesh has a grid spacing of $0.02c$ in the radial and axial directions and an azimuthal spacing of $0.33°$. Figure 11 shows the mesh system used, along with a sample flow-field to demonstrate the quality of the simulations. Computations were also run on a finer grid with $257 \times 201 \times 101$ points for the blade and $180 \times 264 \times 228$ points for background mesh for the $V_\infty = 7$ m/s configuration. The resulting integrated loads and pressure coefficients were confirmed to differ by less than 3%.

Figure 12 compares the predicted integrated thrust and torque to experimental data. As was the case for 2D simulations, solutions are unsteady, and to account for this variability, the current plot as well as several subsequent plots in the paper are shown with error bars indicating the range of values attained. At $V_\infty = 7$ m/s, where the flow stays attached to the turbine blades, both simulations are able to capture the integrated quantities equally well. For higher wind speeds, the accuracy of the correlations decreases, but the overall the trend is well captured. Solutions obtained using the transition model differ from the fully turbulent simulations only at two middle wind speeds, $V_\infty = 10$ m/s and $V_\infty = 15$ m/s. A substantial
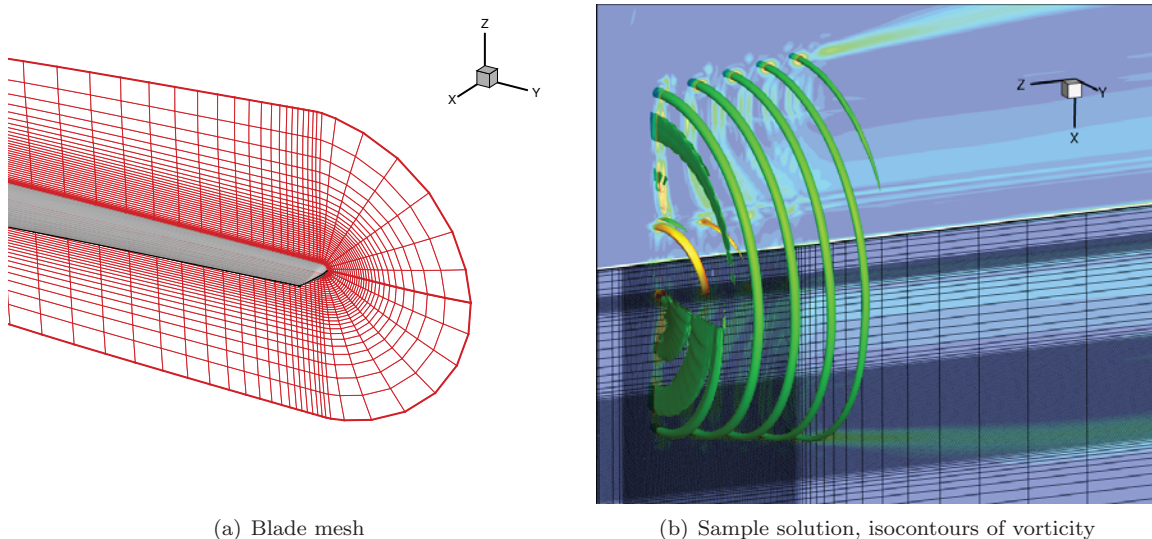
(a) Blade mesh

(b) Sample solution, isocontours of vorticity

Figure 11. Mesh system for NREL wind turbine simulation.

American Institute of Aeronautics and Astronautics
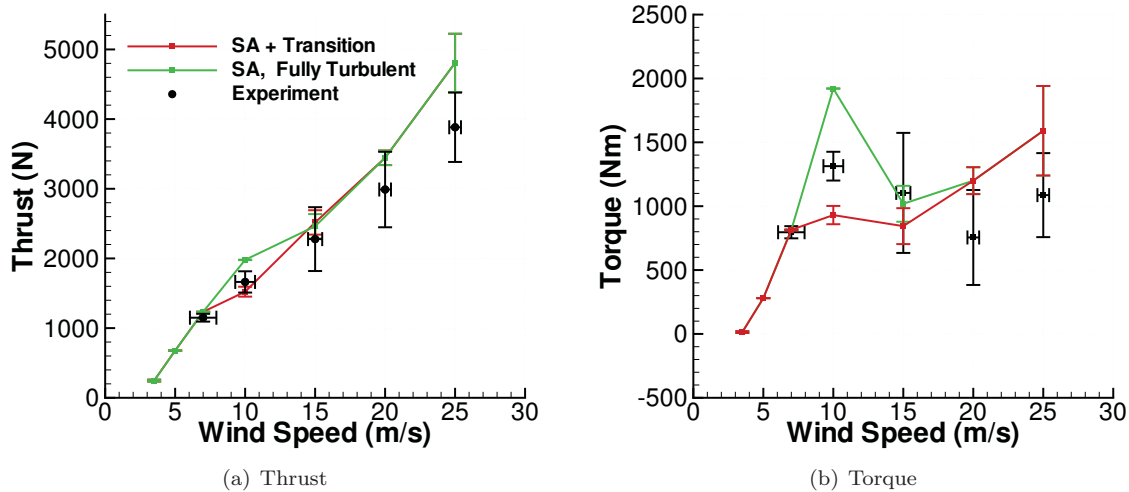
(a) Thrust

(b) Torque

Figure 12. Integrated thrust and torque for NREL wind turbine.

improvement is seen in the prediction of thrust at $V_\infty = 10$ m/s with the use of the transition model. Torque, which is more sensitive to small errors in pressure prediction, is not well captured at this speed.

To further investigate the differences in integrated quantities between the simulations with and without the transition model, sectional thrust and torque coefficients are shown in Fig. 13 for wind speeds of $V_\infty = 7$ m/s, 10 m/s, and 15 m/s. Thrust and torque coefficients are defined by

$$C_T = \frac{T}{\rho \pi R^2 V_{\text{tip}}^2} \tag{1}$$

and torque coefficient defined by

$$C_Q = \frac{Q}{\rho \pi R^3 V_{\text{tip}}^2} \tag{2}$$

where T is the sectional thrust, ρ is freestream density, V_{tip} is the tip velocity, and Q is sectional torque. Unsurprisingly, there is close agreement between the transition model and fully turbulent simulation for the case at $V_\infty = 7$ m/s where the flow stays attached. At $V_\infty = 10$ m/s, the case with the transition model indicates the presence of flow separation through most of the mid span, while the fully turbulent simulation does not show this behavior, accounting for the differences in integrated loads shown earlier. At $V_\infty = 15$ m/s, both simulations show decreased loads through most of the span because of flow separation. The fully turbulent and the transition model results differ substantially in the sectional torque in the outboard regions, and as a result the fully turbulent simulation predicts a slightly higher integrated torque at this wind speed. At higher wind speeds (not shown), the profiles for the fully turbulent and the transition model cases show comparable trends.

A more detailed validation of the current methodology is achieved by comparing the predicted pressure coefficient with and without the use of transition model to available experimental data. The pressure coefficient is computed as:

$$C_p = \frac{P - P_\infty}{\frac{1}{2}\left[M_{\text{FS}}^2 + \left(M_{\text{tip}}\frac{r}{R}\right)^2\right]}, \tag{3}$$

where P is the local static pressure, P_∞ is the pressure in the free stream, M_{FS} is the free stream Mach number, M_{tip} is the rotor tip Mach number, R is the rotor radius, and r is the spanwise coordinate at which the pressure coefficient is evaluated.

Pressure coefficient distributions at $V_\infty = 7$ m/s are shown in Fig 14 at four different spanwise locations. At this wind speed, the flow remains attached across the turbine blade, and the results with and without the use of transition model compare well with the experimental pressure data. The use of the transition model
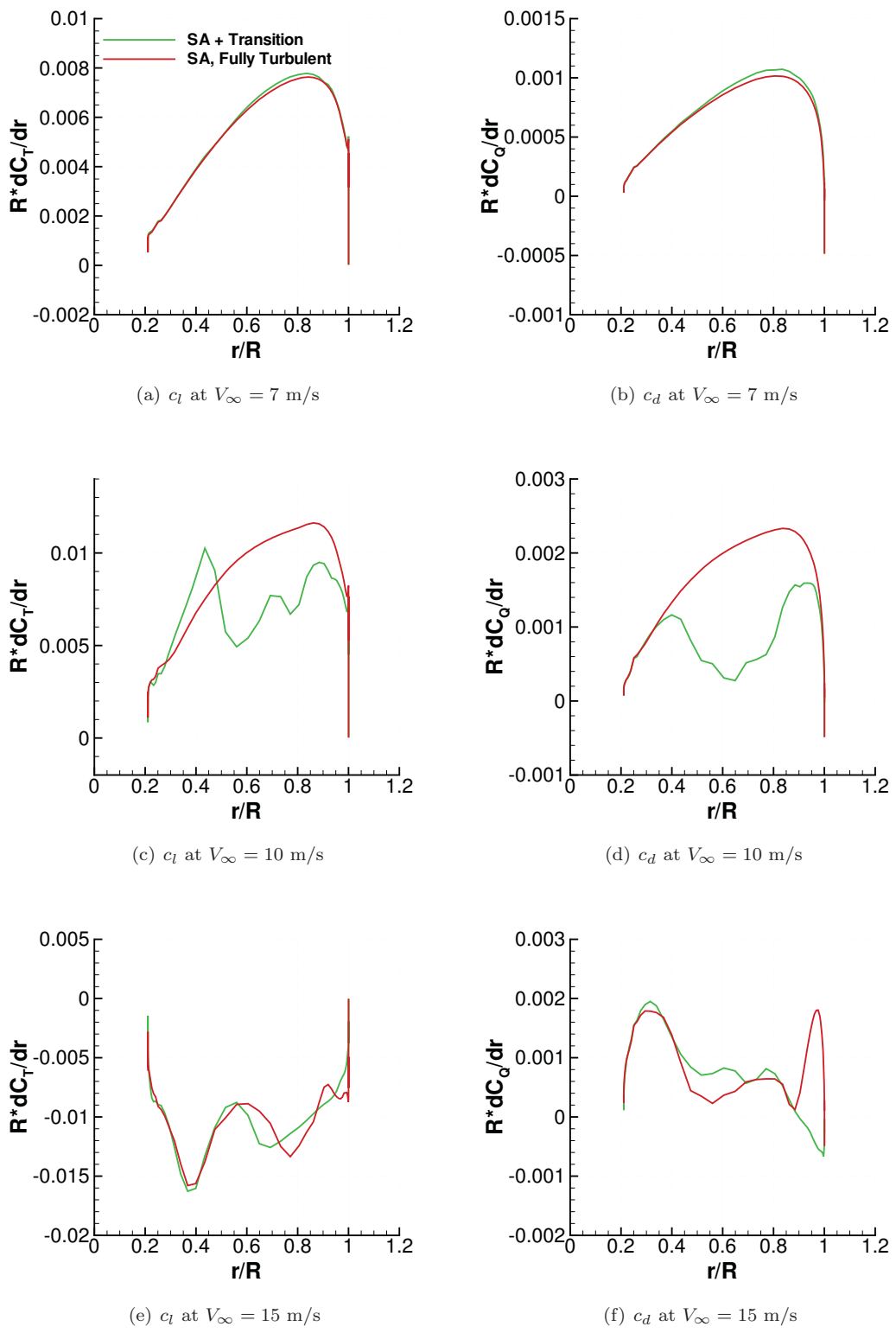
American Institute of Aeronautics and Astronautics

(a) c_l at $V_\infty = 7$ m/s

(b) c_d at $V_\infty = 7$ m/s

(c) c_l at $V_\infty = 10$ m/s

(d) c_d at $V_\infty = 10$ m/s

(e) c_l at $V_\infty = 15$ m/s

(f) c_d at $V_\infty = 15$ m/s

Figure 13. Spanwise load distributions with and without the transition model for NREL wind turbine.

predicts the presence of a separation bubble near the mid-chord region at both upper and lower surface of the airfoil at all spanwise locations. This leads to a small deviation in the pressure distribution between the
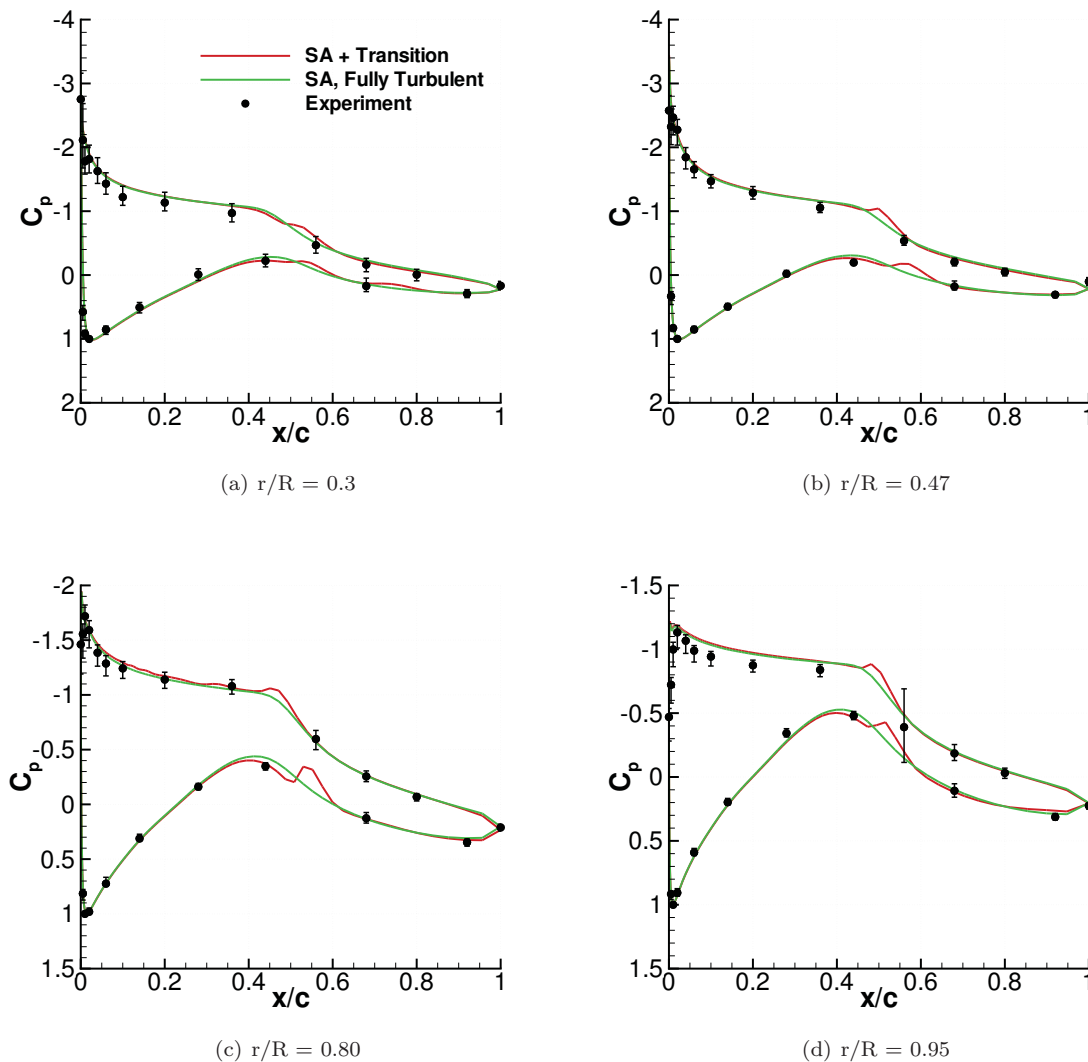
American Institute of Aeronautics and Astronautics

(a) r/R = 0.3

(b) r/R = 0.47

(c) r/R = 0.80

(d) r/R = 0.95

Figure 14. Pressure coefficient distributions for NREL wind turbine, $V_\infty = 7m/s$.

two simulations. Although the available experimental data is insufficient to confirm the correctness of this prediction, this feature is very similar to that observed in the S809 airfoil.

Sectional pressure coefficients at $V_\infty = 10$ m/s, where the flow physics is dominated by transitional effects, are shown in Fig.15. Fully turbulent simulations lead to significant errors in the prediction of pressure on the upper surface at 47% and 95% spanwise locations, whereas the transition model correctly captures the nearly flat pressure distribution that suggests separation at the leading edge. However, the simuation with the transition model shows slightly poorer prediction at 80% spanwise location. Nonetheless, the use of the transition model leads to an overall improvement at this wind speed.

At $V_\infty = 15$ m/s, the computational results are nearly identical with and without the transition model at the inboard span locations shown in Figs. 16(a) and 16(b). At these locations, neither model is able to capture the pressure well. At the next station, at 80% span, shown in Fig. 16(c), both models match the data reasonably well. An anomaly appears at the outboard station at 95% span. Here, the transition model predicts that the flow is separated, whereas the experimental C_p distribution indicates otherwise. In this case, the fully turbulent simulation captures the correct pressure.

Results for pressures at $V_\infty = 20$ m/s and $V_\infty = 25$ m/s are shown in Figures 17 and 18 respectively. At these speeds, the flow is completely separated. There is little difference in performance between the fully turbulent simulations and those using the transition model, and the results compare reasonably well with
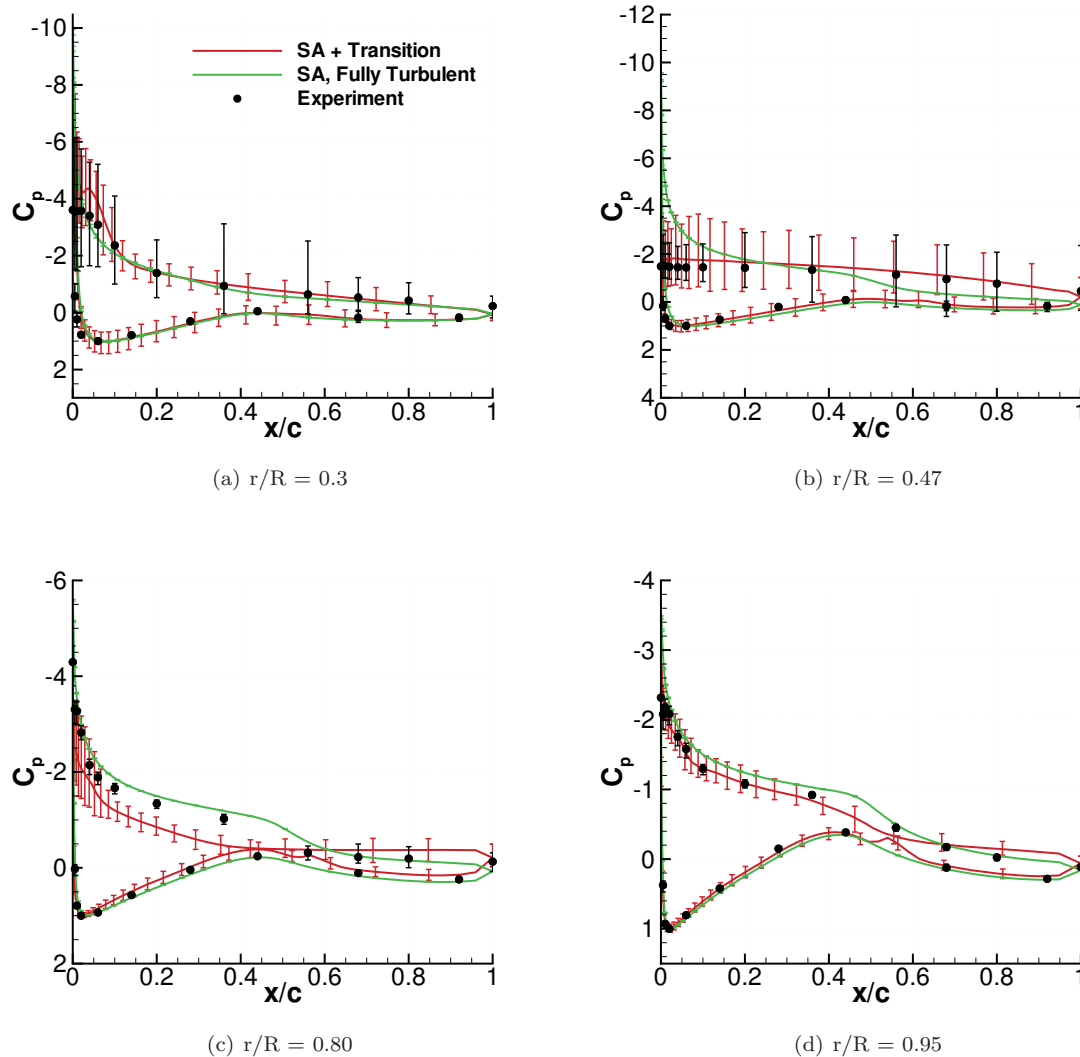
American Institute of Aeronautics and Astronautics

(a) r/R = 0.3

(b) r/R = 0.47

(c) r/R = 0.80

(d) r/R = 0.95

Figure 15. Pressure coefficient distributions for NREL wind turbine, $V_\infty = 10$m/s.

the experimental data.

A more complete picture of the surface pressure is obtained from plots of pressure contours (normalized by freestream pressure) over the blade surface. Figure 19 compares the surface pressure distribution for the simulation with and without the transition model at wind speeds of 7, 10, 15 and 20 m/s. Note that the surfaces are named based on the orientation of the airfoil, which means that the surface referred to as "lower" faces the wind and "upper" faces away. This notation is used consistently in the paper. As observed before, the most significant difference with the use of transition model arises at $V_\infty = 10$ m/s.

Further examination of the effect of the transition model on the flow-field is performed by examining skin friction which is defined as:

$$c_f = \frac{2}{Re_{\text{tip}}} \frac{\partial V_{\text{rot}}}{\partial n} \frac{1}{M_{\text{tip}}} \tag{4}$$

where Re_{tip} is the Reynolds number based on tip velocity, V_{rot} is the velocity magnitude in a reference frame rotating with the blade, and n is the direction normal to the blade surface. Figure 20 shows the skin friction contours (normalized using tip speed and freestream density) along with velocity streamlines. The plots are obtained from solution values located one grid cell off the blade surface. At $V_\infty = 7$ m/s, the transition model predicts the presence of a separation bubble around the mid-chord region through out the
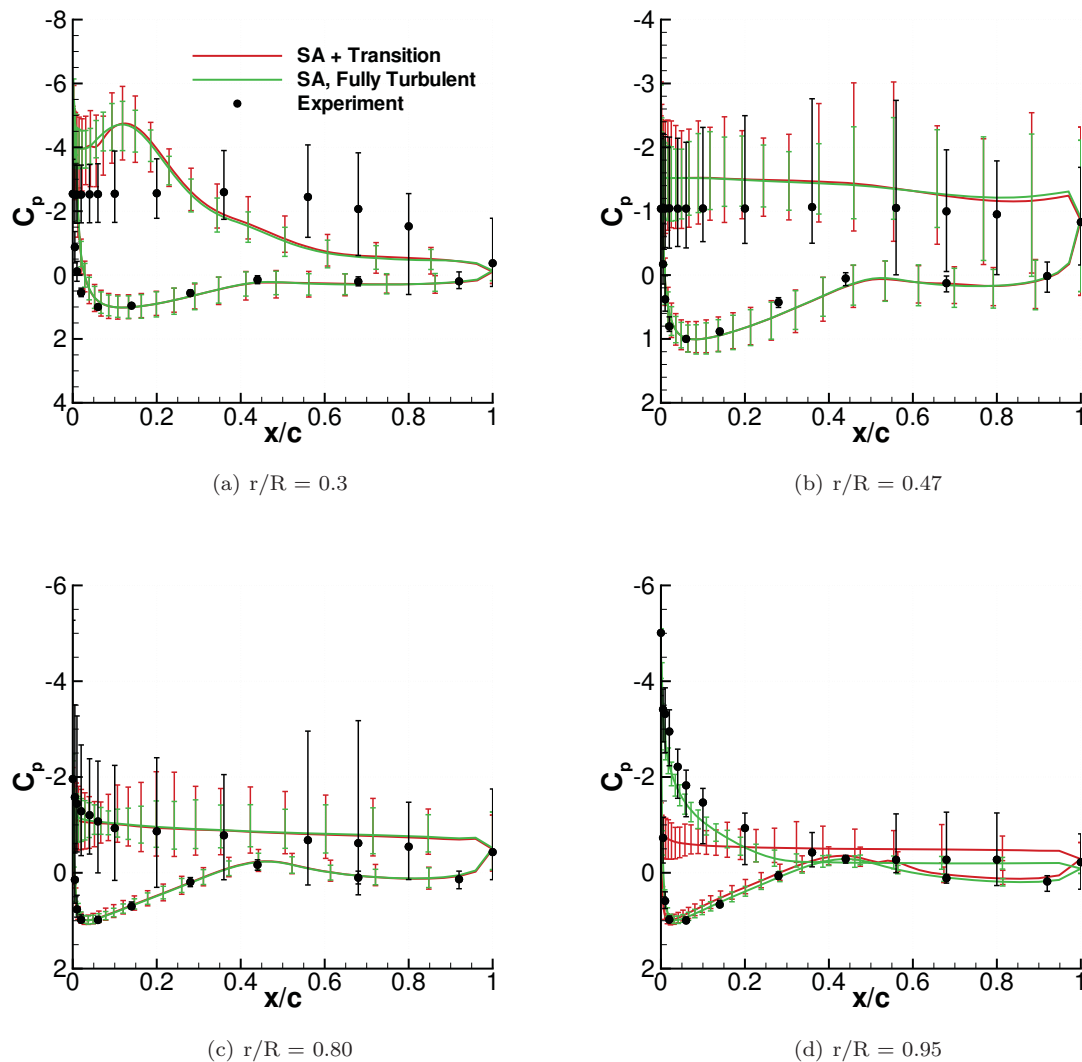
American Institute of Aeronautics and Astronautics

(a) r/R = 0.3

(b) r/R = 0.47

(c) r/R = 0.80

(d) r/R = 0.95

Figure 16. Pressure coefficient distributions for NREL wind turbine, $V_\infty = 15$m/s.

span, which appears as an interruption to the otherwise parallel chordwise flow across the span of the blade. Skin friction in this transitional region is negative due to reversed flow adjacent to the blade surface.

The plots for the 10 m/s case, shown in Figs. 20(c) and 20(d), reveal that there is considerable flow separation over the entire upper surface with the use of transition model. The turbulent simulation, on the other hand, predicts that the separated region is confined to the trailing edge of the upper surface, where the S809 separation ramp is located. Accordingly, the surface skin friction contours for the transitional case reveal a feature-rich distribution of viscous stress which is missing in the fully turbulent case. It has to be mentioned that the image shown is a single time snapshot of a highly unsteady flow, so the features shown do not describe the fluid effect on viscous forces completely.

At $V_\infty = 15$ m/s, transition is predicted in the inboard region of the lower surface. The flow is fully separated on the upper surface for the both simulations. However, the fully turbulent simulation shows a small attached region towards the tip of the upper surface that contributes to discrepancy in the integrated torque prediction described earlier in this section. For $V_\infty = 20$ m/s, the flow is fully separated and there are no sharp changes in skin friction indicative of transition.

Contours of eddy viscosity are shown in Figure 21. The effect of the transition model for the $V_\infty = 7$ m/s case, shown in Figure 21(a) and 21(b) are qualitatively similar to the 2D cases of Figure 4. Laminar flow is expected in the front half of the airfoil, and in this region the eddy viscosity grows slowly when the transition
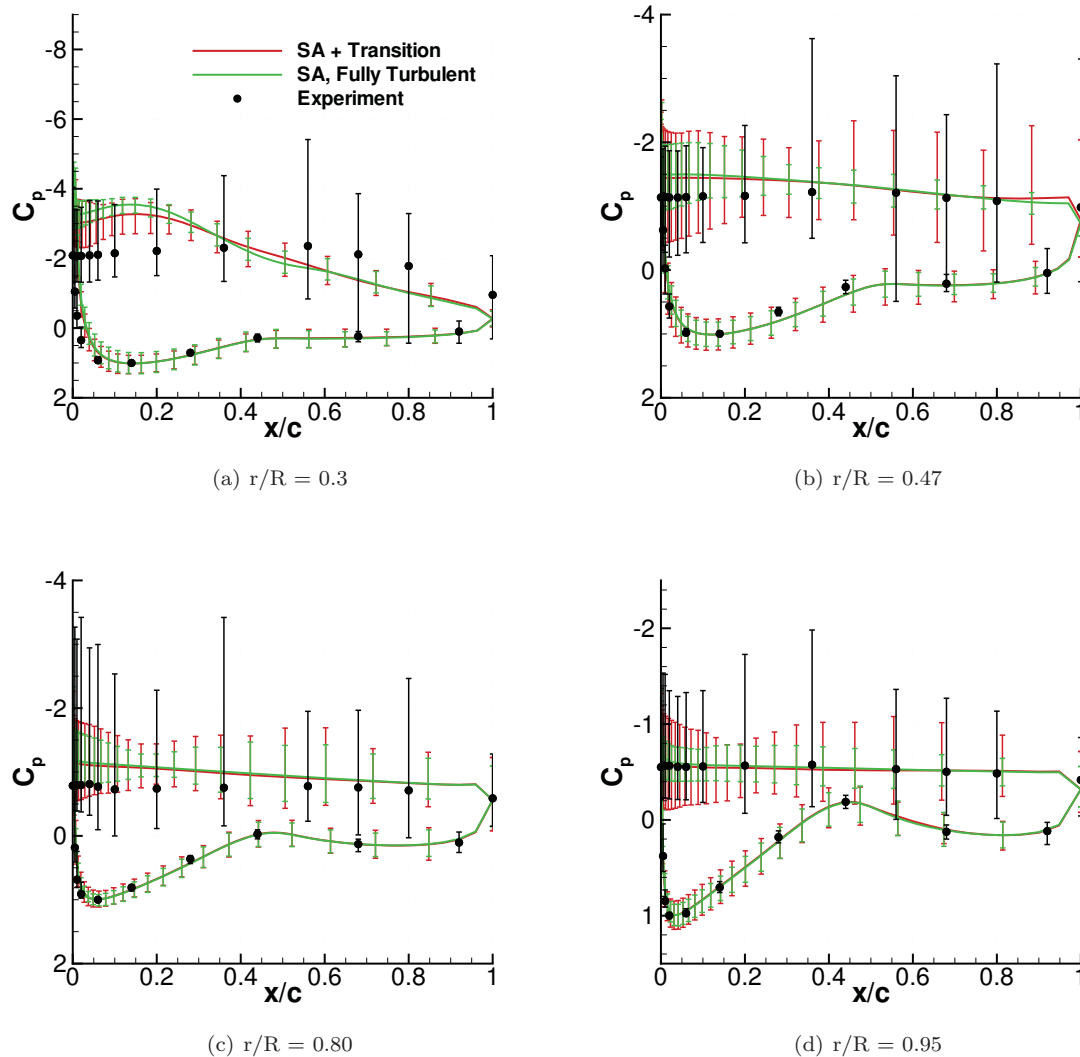
American Institute of Aeronautics and Astronautics

(a) r/R = 0.3

(b) r/R = 0.47

(c) r/R = 0.80

(d) r/R = 0.95

Figure 17. Pressure coefficient distributions for NREL wind turbine, $V_\infty = 20$m/s.

model is applied. The fully turbulent simulation predicts a strong growth of eddy viscosity throughout the surface of the airfoil and in the wake as a result. For $V_\infty = 10$ m/s, shown in Figs. 21(c) and 21(d), the transition model predicts a faster growth rate of eddy viscosity. As in the the 2D airfoil in Fig. 5, the transition model is seen to generate lower levels of viscous damping and thus an earlier flow separation. Contours at $V_\infty = 20$ m/s are shown in Figures 21(e) and 21(f). Large separations are seen in these plots, and the magnitude of eddy viscosity increases radically with increasing wind speed, leading to high levels of mixing characteristic of turbulent flows.

V.   Conclusions

In this work, the $\gamma - \overline{Re_{\theta t}} - SA$ transition model has been used in a RANS solver with overset grid methodology for the analysis of flows over wind turbine airfoils and rotor blades. In situations for which flow remains completely attached or massively separated, the transition model qualitatively and quantitatively exhibits the same behavior as the fully turbulent model. When incipient and small separation regions are present, the transition model is seen to significantly improve the quality of the solution. This is seen in the 2D validation of the S827 airfoil, where the transition model is able to capture the double slope of the lift curve
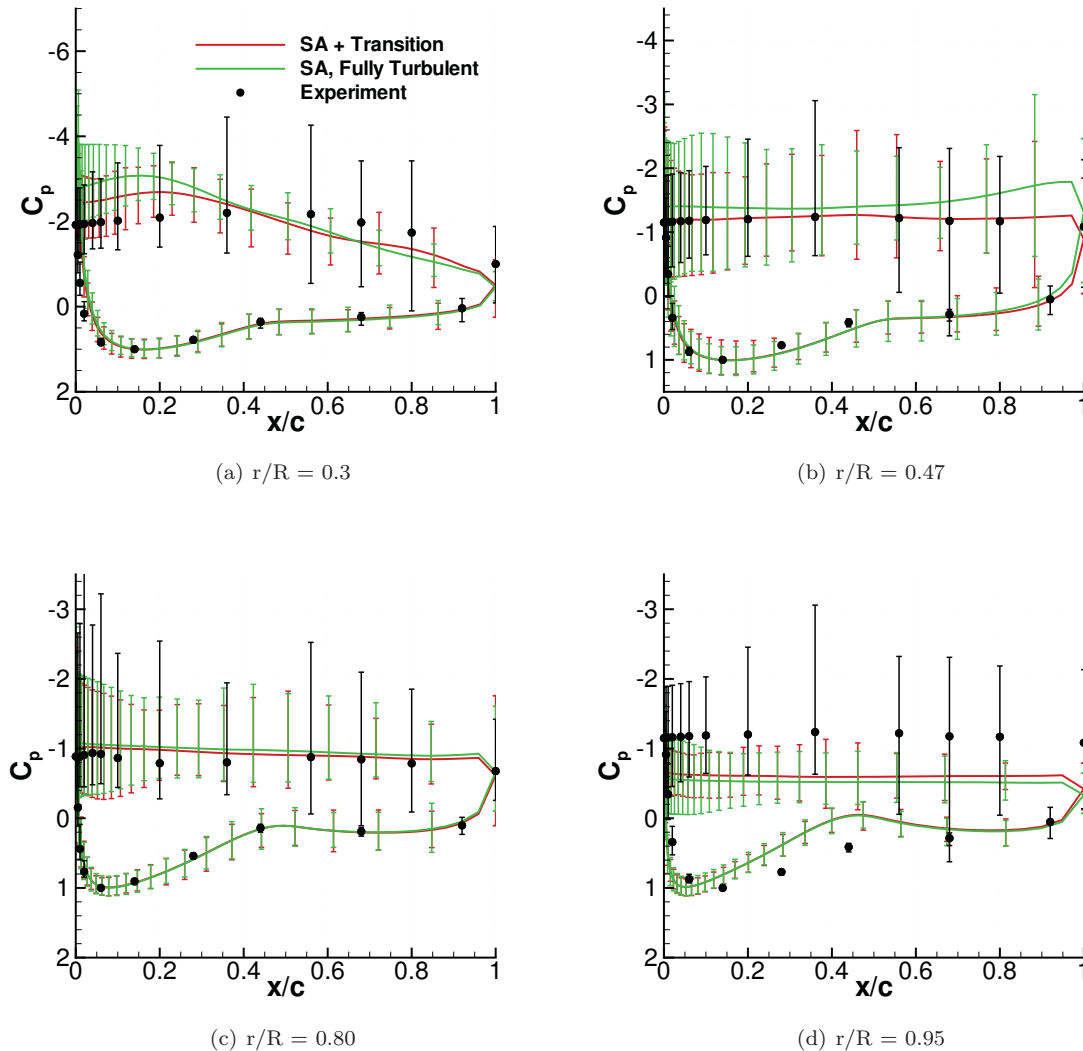
American Institute of Aeronautics and Astronautics

Figure 18. Pressure coefficient distributions for NREL wind turbine, $V_\infty = 25$m/s.

and match the experimentally determined surface pressure coefficient. The transition model also greatly improves the accuracy of the 2D S809 simulation in the post-stall regime, another case that involves limited flow separation. In the simulations of the NREL Phase VI wind turbine, the transition model substantially improves the prediction of quantities at $V_\infty = 10$ m/s. The continued need for improved modeling is evident in the discrepancies in predicting the aerodynamic characteristics of the S827 airfoil in the middle range of angles of attack as well as the considerable errors seen in the wind turbine simulations involving separation.

Accurate aerodynamic modeling of wind turbine flows remains a challenge in flow regimes that are defined by transition and separation. As LES and DNS will continue to be infeasible for industrial applications in the next decade, accurate RANS based models will remain desirable for these problems. Further development of these models requires more highly refined experimental datasets as well as DNS results in simpler, isolated situations, such that the effect of rotation, secondary flows and turbulence anisotropy can be better characterized, leading to improved predictions of transition and separation.

(a) $V_\infty = 7$m/s, without transition

(b) $V_\infty = 7$m/s, with transition

(c) $V_\infty = 10$m/s, without transition

(d) $V_\infty = 10$m/s, with transition

(e) $V_\infty = 15$m/s, without transition

(f) $V_\infty = 15$m/s, with transition

(g) $V_\infty = 20$m/s, without transition

(h) $V_\infty = 20$m/s, with transition
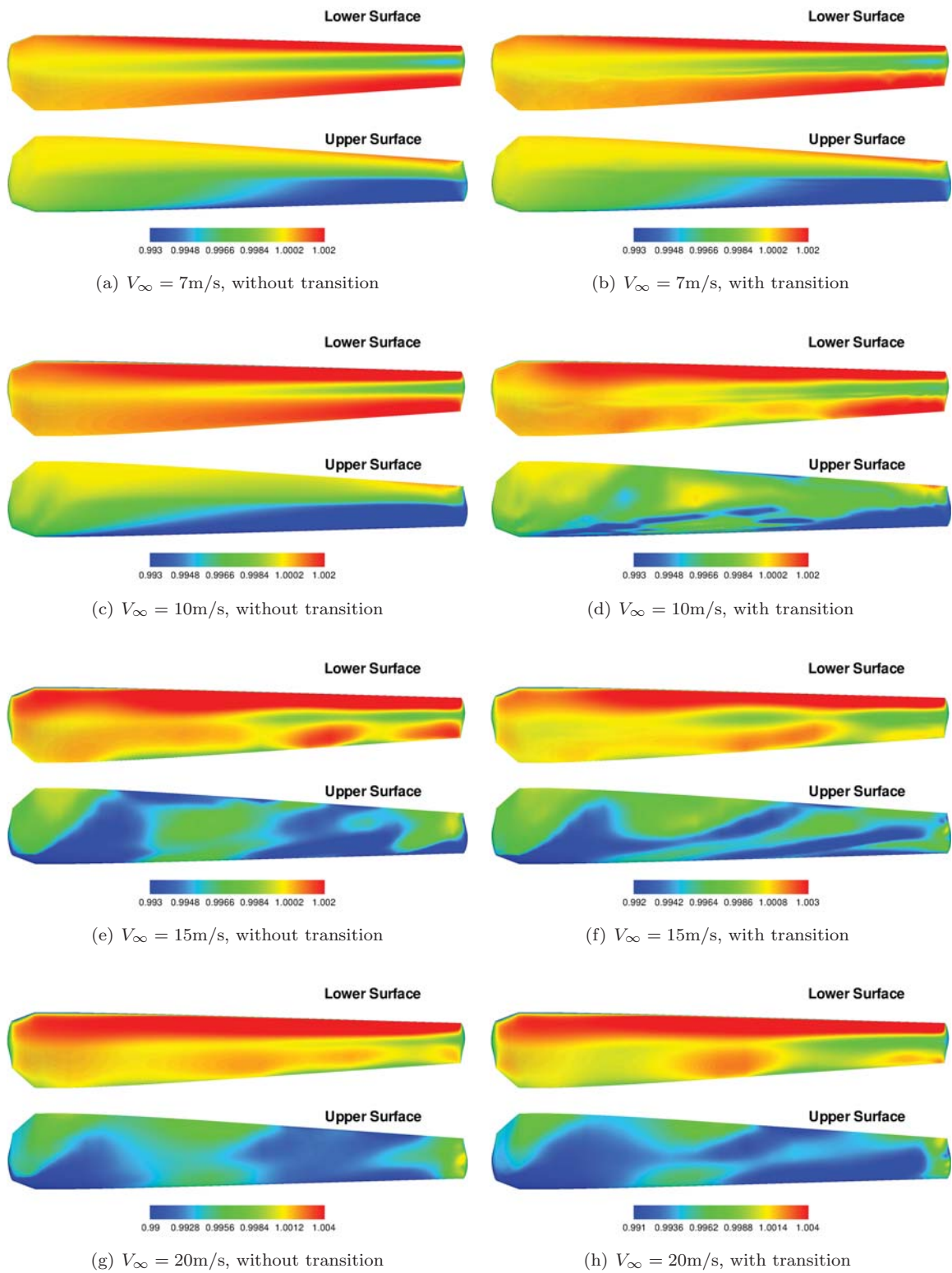
Figure 19. Surface pressure contours for NREL wind turbine.

American Institute of Aeronautics and Astronautics

(a) $V_\infty = 7$m/s, without transition

(b) $V_\infty = 7$m/s, with transition

(c) $V_\infty = 10$m/s, without transition

(d) $V_\infty = 10$m/s, with transition

(e) $V_\infty = 15$m/s, without transition

(f) $V_\infty = 15$m/s, with transition

(g) $V_\infty = 20$m/s, without transition

(h) $V_\infty = 20$m/s, with transition
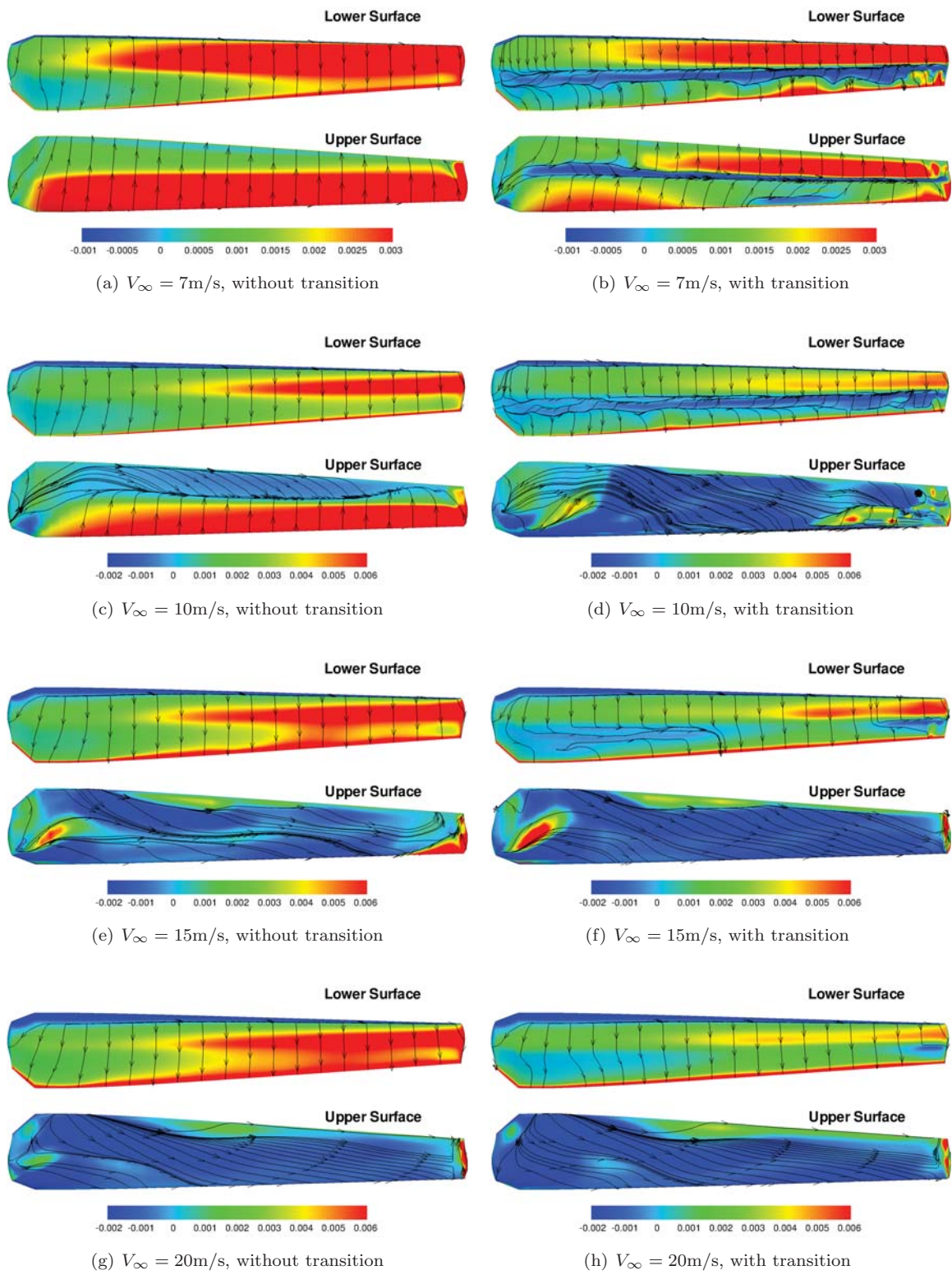
Figure 20. Contours of skin friction along with surface streamlines for NREL wind turbine.

American Institute of Aeronautics and Astronautics

(a) $V_\infty = 7$m/s, without transition

(b) $V_\infty = 7$m/s, with transition

(c) $V_\infty = 10$m/s, without transition

(d) $V_\infty = 10$m/s, with transition

(e) $V_\infty = 20$m/s, without transition

(f) $V_\infty = 20$m/s, with transition
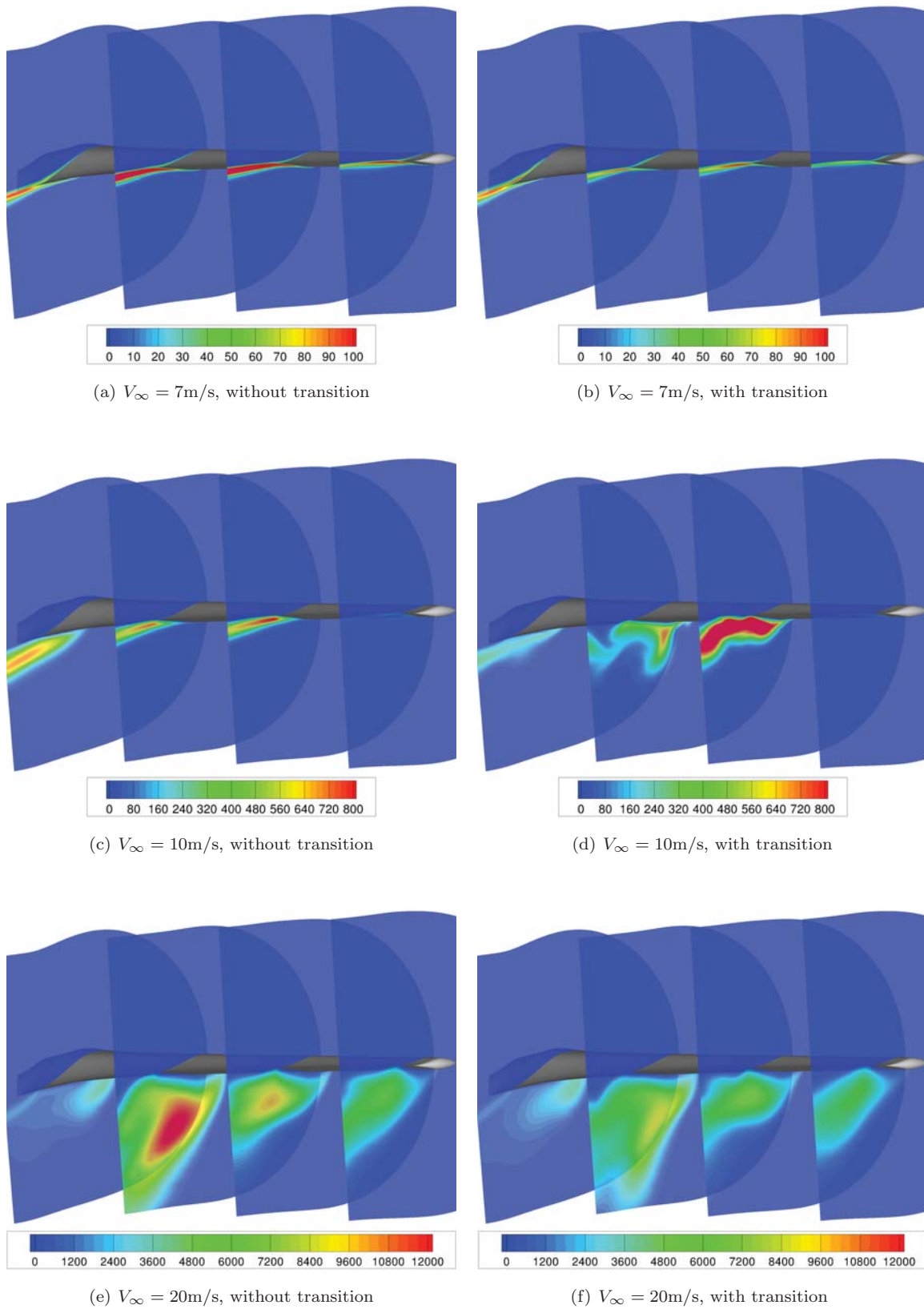
Figure 21. Sectional eddy viscosity contours.

American Institute of Aeronautics and Astronautics

VI. Acknowledgement

A. Description of the $\gamma - \overline{Re_{\theta t}}$ transition model

The original $\gamma - \overline{Re_{\theta t}}$ transition model was developed by Langtry et al.[19] for use with the SST-$k - \omega$ turbulence model. One advantage of this model over many other transition models is that $\gamma - \overline{Re_{\theta t}}$ does not require the integration of a boundary layer followed by a search for critical Re_θ at which transition onset begins. Furthermore, because this model allows intermittency to vary across the boundary layer, it is able to capture transition triggered by a laminar separation bubble without need for further correction. This is particularly advantageous in low speed flows, where separation bubbles are frequently the cause of transition. The $\gamma - \overline{Re_{\theta t}}$ model is correlation-based and provides a convenient framework wherein users may insert proprietary or internal correlations.

The $\gamma - \overline{Re_{\theta t}} - SA$ model, introduced by Medida et al.[22] adapts this method to work with the one equation Spalart-Allmaras turbulence model. Because the $\gamma - \overline{Re_{\theta t}} - SA$ model has been introduced recently, and because its implementation in OVERTURNS is original, the present work performs additional validation to confirm its credibility in transitional flows such as those seen in wind turbine applications.

In addition to the RANS equation and turbulence model equation, the $\gamma - \overline{Re_{\theta t}} - SA$ model requires the solution of two transport equations. The first is for intermittency, γ, a quantity which varies from zero to one and represents the probability of turbulent flow at a given location. The second is for the transition momentum thickness Reynolds number $\overline{Re_{\theta t}}$, the purpose of which is to convect the effects of turbulence intensity from the freestream into the boundary layer.

When coupled with $\gamma - \overline{Re_{\theta t}} - SA$, the equation for the Spalart-Allmaras variable becomes

$$\frac{D\tilde{\nu}}{Dt} = \tilde{P}_\nu - \tilde{D}_\nu + \frac{1}{\sigma}\left[\nabla \cdot ((\nu + \tilde{\nu})\nabla\tilde{\nu}) + c_{b2}(\nabla\tilde{\nu})^2\right] \tag{5}$$

where the source terms $\tilde{P}_\nu$ and $\tilde{D}_\nu$ are modified from the original turbulence model to depend on intermittency as follows:

$$\tilde{P} = \gamma_{eff}P_\nu, \qquad \tilde{D}_\nu = \max(\min(\gamma, \beta), 1.0)D_\nu, \qquad \beta = 0.5 \tag{6}$$

The model parameter γ_{eff} will be defined below. The original source terms P_ν and D_ν and remaining closure constants are those given by the Spalart-Allmaras model:

$$\nu_t = \tilde{\nu}_t f_{\nu 1}, \qquad f_{\nu 1} = \frac{\chi^3}{\chi^3 + c_{\nu 1}^3}, \qquad \chi = \frac{\tilde{\nu}}{\nu} \tag{7}$$

$$P_\nu = c_{b1}\tilde{\Omega}\tilde{\nu} \quad \text{and} \quad D_\nu = c_{w1}f_w\left[\frac{\tilde{\nu}}{d}\right]^2 \tag{8}$$

$$\tilde{\Omega} = \Omega + \frac{\tilde{\nu}}{\kappa^2 d^2}f_{\nu 2}, \qquad f_{\nu 2} = 1 - \frac{\chi}{1 + \chi f_{\nu 1}} \tag{9}$$

$$f_w = g\left[\frac{1 + c_{w3}^6}{g^6 + c_{w3}^6}\right]^{\frac{1}{6}}, \qquad g = r + c_{w2}(r^6 - r), \qquad r = \frac{\tilde{\nu}}{\tilde{\Omega}\kappa^2 d^2} \tag{10}$$

$$c_{b1} = 0.1355, \; \sigma = \frac{2}{3}, \; \kappa = 0.41, \; c_{w1} = \frac{c_{b1}}{\kappa^2} + \frac{1 + c_{b2}}{\sigma}, \; c_{w2} = 2.0, \; c_{\nu 1} = 7.1 \tag{11}$$

The transport equation for intermittency is

$$\frac{D(\rho\gamma)}{Dt} = P_\gamma - D_\gamma + \frac{\partial}{\partial x_j}\left[\left(\mu + \frac{\mu_t}{\sigma_f}\right)\frac{\partial\gamma}{\partial x_j}\right] \tag{12}$$

with auxillary equations given by

$$P_\gamma = F_{\text{length}}c_{a1}\rho S[\gamma F_{\text{onset}}]^{0.5}(1.0 - c_{e1}\gamma) \tag{13}$$

$$D_\gamma = c_{a2}\rho\Omega\gamma F_{\text{turb}}(c_{e2}\gamma - 1.0) \tag{14}$$

$$F_{\text{onset}} = \max(F_{\text{onset2}} - F_{\text{onset3}}, 0) \tag{15}$$

$$F_{\text{onset1}} = \frac{Re_\nu}{2.193 Re_{\theta c}} \tag{16}$$

$$F_{\text{onset2}} = \min(\max(F_{\text{onset1}}, F_{\text{onset1}}^4), 2.0) \tag{17}$$

$$F_{\text{onset3}} = \max\left(1 - \left(\frac{R_T}{2.5}\right)^3, 0\right) \tag{18}$$

$$F_{\text{turb}} = e^{\left(-\frac{R_T}{4}\right)^4} \tag{19}$$

$$Re_\nu = \frac{\rho d^2 S}{\mu}, \qquad Re_T = \frac{\mu_t}{\mu} \tag{20}$$

The transport equation for critical momentum thickness Reynolds number is

$$\frac{D(\rho\overline{Re_{\theta t}})}{Dt} = P_{\theta t} + \frac{\partial}{\partial x_j}\left[\sigma_{\theta t}(\mu + \mu_t)\frac{\partial\overline{Re_{\theta t}}}{\partial x_j}\right] \tag{21}$$

with auxillary relations given by

$$P_{\theta t} = c_{\theta t}\frac{\rho}{t}(Re_{\theta t} - \overline{Re_{\theta t}})(1.0 - F_{\theta t}) \tag{22}$$

$$F_{\theta t} = \min\left(\max\left(F_{\text{wake}}e^{-\left(\frac{d}{\delta}\right)^4}, 1.0 - \left(\frac{\gamma - 1/c_{e2}}{1.0 - 1/c_{e2}}\right)^2\right), 1.0\right) \tag{23}$$

A set of correlations for critical momentum thickness Reynolds number is:

$$Re_{\theta t} = \begin{cases} (1173.51 - 589.428 Tu + \frac{0.2196}{Tu^2})F(\lambda_\theta), & Tu \le 1.3 \\ 331.50[Tu - 0.5658]^{-0.671}F(\lambda_\theta), & Tu > 1.3 \end{cases} \tag{24}$$

$$F(\lambda_\theta) = \begin{cases} 1 - [-12.986\lambda_\theta - 123.66\lambda_\theta^2 - 405.689\lambda_\theta^3]\, e^{\left[\frac{Tu}{1.5}\right]^{1.5}}, & \lambda_\theta \le 0 \\ 1 + 0.275[1 - e^{[-35.0\lambda_\theta]}]e^{\left[\frac{Tu}{0.5}\right]} & \lambda_\theta > 0 \end{cases} \tag{25}$$

$$\lambda_\theta = \frac{\rho\theta^2}{\mu}\frac{dU}{ds} \tag{26}$$

$$\theta_{BL} = \frac{\overline{Re_{\theta t}}\mu}{\rho U}; \qquad \delta_{BL} = 7.5\theta_{BL}; \ \delta = \frac{50\omega d}{U}\delta_{BL} \tag{27}$$

and the model constants are

$$c_{e1} = 1.0; \quad c_{q1} = 2.0; \quad c_{e2} = 50.0; \quad c_{a2} = 0.06; \quad \sigma_f = 1.0 \tag{28}$$

$$c_{\theta t} = 1.0; \quad \sigma_{\theta t} = 2.0 \tag{29}$$

To improve the prediction of transition due to laminar separation bubble, the following correction is used.

$$\gamma_{\text{sep}} = \min\left(s_1\max\left[0, \left(\frac{Re_\nu}{3.235 Re_{\theta c}}\right) - 1\right]F_{\text{reattach}}, 2.0\right)F_{\theta t} \tag{30}$$

$$\gamma_{\text{eff}} = \max(\gamma, \gamma_{\text{sep}}) \tag{31}$$

$$F_{\text{reattach}} = e^{-\left(\frac{R_T}{20}\right)^4}, \quad \text{and} \quad s_1 = 2.0 \tag{32}$$

American Institute of Aeronautics and Astronautics

References

[1] U.S. Department of Energy, "20% Wind Energy by 2030, Increasing Wind Energy's Contribution to U.S. Electricity Supply," DOE/GO-102008-2567, 2008.

[2] M. O. Hansen, *Aerodynamics of Wind Turbines, 2nd Ed.,* Earthscan, 2008.

[3] J. G. Leishman, "Challenges in Modelling the Unsteady Aerodynamics of Wind Turbines", *Wind Energy*, Vol. 5, No. 2, pp. 85–132, 2002.

[4] D. Simms, S. Schreck, M. Hand, and L.J. Fingersh, "NREL Unsteady Aerodynamics Experiment in the NASA-Ames Wind Tunnel: A Comparison of Predictions to Measurements", NREL/TP-500-29494, 2001.

[5] M. M. Hand, D. A. Simms, L. J. Fingersh, D. W. Jager, J. R. Cotrell, S. Schreck, and S. M. Lawood, "Unsteady Aerodynamics Experiment Phase VI: Wind Tunnel Test Configurations and Available Data Campaigns", NREL/TP-500-29955, 2001.

[6] N. N. Sørensen, J. A. Michelsen, and S. Schreck, "Navier-Stokes Predictions of the NREL Phase VI Rotor in the NASA Ames 80 ft × 120 ft Wind Tunnel", *Wind Energy*, Vol. 5, No. 2, pp. 151–169 2002.

[7] E. P. N. Duque, M. D. Burklund, and W. Johnson, "Navier-Stokes and Comprehensive Analysis Performance Predictions of the NREL Phase VI Experiment," *Journal of Solar Energy Engineering*, Vol. 125, No. 4, 2003.

[8] M. A. Potsdam and D. J. Mavriplis, "Unstructured Mesh CFD Aerodynamic analysis of the NREL Phase VI Rotor", AIAA Aerospace Sciences Meeting, Orlando, FL, January 2009.

[9] P. Devinant, T. Laverne, and J. Hureau, "Experimental study of wind-turbine airfoil aerodynamics in high turbulence," *Journal of Wind Engineering and Industrial Aerodynamics*, Vol. 90, No. 6, pp. 689707, June 2002.

[10] R. Michel, "Etude de la Transition sur les Profiles d'Aile," ONERA Report 1/1578A, 1951.

[11] J. Moran, *An Introduction to Theoretical and Computational Aerodynamics*, Dover Publications, Mineola, New York, 1984.

[12] R. Eppler, "A Computer Program for the Design and Analysis of Low-Speed Airofils", NASA Langley Research Center, NASA-TM-80210, N80-29254, 1980.

[13] D. M. Somers, Design and Experimental Results for the S809 Airfoil. NREL/SR-440-6918, Jan. 1997.

[14] D. M. Somers, Design and Experimental Results for the S827 Airfoil. Airfoils, Inc., 1999.

[15] R. J. A. Howard, M. Alam, and N. D. Sandham, "Two-Equation Turbulence Modelling of a Transitional Separation Bubble", *Flow, Turbulence and Combustion*, Vol. 63, 1999.

[16] A. M. O. Smith and N. Gamberoni, "Transition Pressure Gradient and Stability Theory," Douglas Aircraft Company, Long Beach, California, Rep. ES 26388, 1956.

[17] J. L. Van-Ingen, "A Suggested Semi-Empirical Method for the Calculation of the Boundary Layer Transition Region," Univ. of Deft, Dept. Aerospace Engineering, Rep. VTH-74, 1956.

[18] D. D. Pasquale, A. Rona, and S. J. Garrett, "A Selective Review of CFD Transition Models", 39th AIAA Fluid Dynamics Conference, San Antonio, TX, June 2009.

[19] R. B. Langtry and F. R. Menter, "Transition Modeling for General CFD Applications in Aeronautics", 43rd AIAA Aerospace Sciences Meeting and Exhibit, Reno, Nevada, January 2005.

[20] R. B. Langtry, J. Gola, and F. R. Menter, "Predicting 2D Airfoil and 3D Wind Turbine Rotor Performance using a Transition Model for General CFD Codes", 44th AIAA Aerospace Sciences Meeting and Exhibit, Reno, Nevada, January 2006.

[21] F. R. Menter, "Two-Equation Eddy-Viscosity Turbulence Models for Engineering Application", *AIAA Journal*, Vol. 32, No. 8, pp. 1598–1605, 1994.

[22] S. Medida and J. Baeder, "Numerical Prediction of Static and Dynamic Stall Phenomena using the $\gamma - \overline{Re_{\theta t}}$ Transition Model", American Helicopter Society 67$^{\text{th}}$ Annual Forum, Virginia Beach, VA, May 2011.

[23] P. R. Spalart and S. R. Allmaras, "A One-equation Turbulence Model for Aerodynamic Flows," AIAA Paper 1992-0439, 30th AIAA Aerospace Sciences Meeting and Exhibit, Reno, NV, January 6–9, 1992.

[24] V. K. Lakshminarayan, "Computational Investigation of Micro-Scale Coaxial Rotor Aerodynamics in Hover," Ph.D. dissertation, Department of Aerospace Engineering, University of Maryland at College Park, 2009.

[25] P. E. O. Buelow, D. A. Schwer, J. Feng, C. L. Merkle, "A Preconditioned Dual-Time, Diagonalized ADI scheme for Unsteady Computations," 13th AIAA Computational Fluid Dynamics Conference, Snowmass Village, CO, June 1997.

[26] S. A. Pandya, S. Venkateswaran, and T. H. Pulliam, "Implementation of Preconditioned Dual-Time Procedures in OVERFLOW," 41st AIAA Aerospace Sciences Meeting and Exhibit, Reno, NV, January 2003.

[27] T. Pulliam, and D. Chaussee, "A Diagonal Form of an Implicit Approximate Factorization Algorithm," *Journal of Computational Physics,* Vol. 39, No. 2, pp. 347–363, 1981.

[28] E. Turkel, "Preconditioning Techniques in Computational Fluid Dynamics," *Annual Review of Fluid Mechanics,* Vol. 31, January 1999, pp. 385–416.

[29] Y. Lee *On Overset Grids Connectivity and Vortex Tracking in Rotorcraft CFD*, PhD Dissertation, University of Maryland, College Park, 2008.

American Institute of Aeronautics and Astronautics